

Fabrication of ball-shaped atomic force microscope tips by ion-beam-induced deposition of platinum on multiwall carbon nanotubes

Yung Ho Kahng^{a,e}, Jinho Choi^{a,b}, Kwanghoon Jeong^{a,c}, Byong Chon Park^a, Dal-Hyun Kim^a, Joon Lyoo^b, Jae-Joon Lee^{c,*}, Haiwon Lee^d, Takhee Lee^e, Sang Jung Ahn^{a,**}

^a Korea Research Institute of Standards and Science, Daejeon 305-340, Republic of Korea

^b Department of Electrical Engineering, Chungnam National University, Daejeon 305-764, Republic of Korea

^c Department of Applied Chemistry & Department of Advanced Technology Fusion, Konkuk University, Chungju 380-701, Republic of Korea

^d Department of Chemistry, Hanyang University, Seoul 133-791, Republic of Korea

^e Department of Materials Science and Engineering, Gwangju Institute of Science and Technology, Gwangju 500-712, Republic of Korea

ARTICLE INFO

Article history:

Received 3 June 2009

Received in revised form

14 September 2009

Accepted 22 September 2009

PACS:

81.07.-b

Keywords:

Carbon nanotube tip

Atomic force microscopy

Focused ion beam

ABSTRACT

Ball-shaped atomic force microscope (AFM) tips (ball tips) are useful in AFM metrology, particularly in critical dimension AFM metrology and in micro-tribology. However, a systematic fabrication method for nano-scale ball tips has not been reported. We report that nano-scale ball tips can be fabricated by ion-beam-induced deposition (IBID) of Pt at the free end of multiwall carbon nanotubes that are attached to AFM tips. Scanning electron microscopy and transmission electron microscopy analyses were done on the Pt ball tips produced by IBID in this manner, using ranges of Ga ion beam conditions. The Pt ball tips produced consisted of aggregated Pt nano-particles and were found to be strong enough for AFM imaging.

© 2009 Elsevier B.V. All rights reserved.

1. Introduction

Creation of atomic force microscopy (AFM) tips with special shapes has drawn much attention from the research community due to their usefulness in AFM metrology [1–7]. Various shapes such as multiwall carbon nanotube (MWNT)-attached AFM tips (MWNT tips) [1–4], shape-modified MWNT tips [6,7], boot-shaped AFM tips [5], and ball-shaped AFM tips [8–10] have been produced. Among these, ball-shaped AFM tips are interesting due to their usefulness in critical dimension AFM (CD-AFM) metrology [4,5,8], in micro-tribology [9–13], and in measurements of the mechanical properties of biological cells [14]. However, conventional ball tips are produced by attaching glass beads to AFM tips [9,10]. These beads are generally only available in a small range of sizes and are unavailable with nano-scale diameters, so it is not possible to control the ball diameter finely or to fabricate nano-scale ball tips.

Here, we report the formation of a ball-shaped AFM tip by depositing Pt at the free end of an MWNT tip using ion-beam-

induced deposition (IBID). Although various structures have already been produced by IBID [15–18], to the best of our knowledge, a study of Pt ball formation on MWNT tips has not been reported. We present a systematic investigation of Pt ball capping on MWNT tips by IBID. Pt ball growth under various ion beam conditions was monitored *in situ* in a dual-beam focused ion beam machine (FIB) and *ex situ* in a transmission electron microscope (TEM). Pt ball diameter can be controlled finely from tens of nanometers up to 600 nm and the ratio of the ball diameter to tube diameter can be made as large as 8. The Pt ball itself consists of aggregated Pt nano-particles in an amorphous carbon medium. The mechanism of the ball formation is discussed in this work as well. Our method of producing ball tips with finely controlled nanometer-range diameters may broaden the application range of AFM metrology.

2. Experimental details

MWNT tips are produced by attaching MWNTs onto AFM tips using e-beam-induced deposition (EBID) of hydrocarbons in a scanning electron microscope (SEM). In this method, a MWNT cartridge is located on one side and an AFM tip is loaded onto the other side of a nanomanipulator in a SEM. Precisely controlled

* Corresponding author. Tel.: +82 43 840 3580.

** Corresponding author. Tel.: +82 42 868 5609; fax: +82 42 868 5608.

E-mail addresses: jjlee@kku.ac.kr (J.-J. Lee), sjahn@kriss.re.kr (S. J. Ahn).

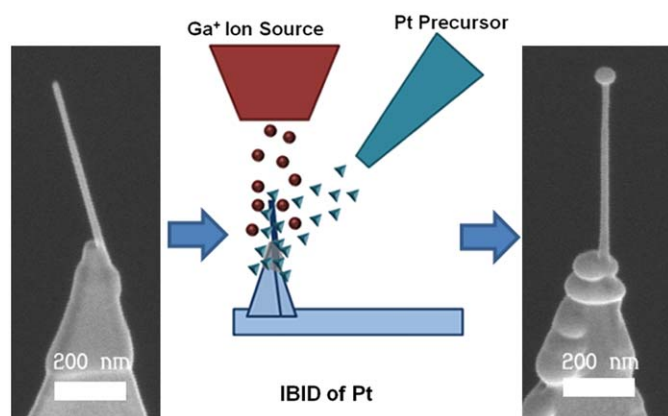


Fig. 1. Illustration of the experimental process of Pt ball tip fabrication. SEM images of an MWNT tip before and after Pt ball capping are shown. The diameter of the Pt ball formed was 60 nm.

movement of the two sides of the manipulator mounts the target MWNT on the apex of an AFM tip, all under observation by SEM. EBID of hydrocarbons is used to attach the MWNT to the AFM tip [19]. A SEM image of a MWNT tip after production is shown in Fig. 1.

After the MWNT tip is fabricated, we use ion-beam-induced deposition (IBID) of Pt in a dual-beam focused ion-beam machine (FIB, Nova 200, FEI, Co.) to deposit Pt on top of the MWNT tips. The precursor gas used was methylcyclopentadienyl (trimethyl) platinum ($C_9H_{16}Pt$). The MWNT was first aligned toward Ga^+ ion beam using the ion-beam-bending process [6] before Pt deposition. During Pt deposition, a gas injection system supplied precursor gas to the sample surface, which was saturated with the adsorbed gas molecules. Pt was deposited by ion-energy-induced breaking of the adsorbed precursor within the illuminated area. If the ion current is not too large, such deposition is ion-beam-limited: that is, the size and energy of the ion beam determines the deposition rate. The ion beam acceleration voltages used were 10, 20, and 30 kV, and nominal ion beam currents were 3, 23, and 10 pA, respectively. We measured the actual ion beam currents using a Faraday cup, and found that they were up to 30% different from the nominal values. Pt deposition was done in steps, with target thicknesses varying from 10 to 200 nm. Choosing a target thickness selected a certain value for the ion beam fluence to the sample, which was precalibrated by the manufacturer of the FIB machine. According to this predetermined target thickness, the FIB exposed the target area to a programmed amount of Ga ion fluence. The deposition pattern used was a circle of 1 μm diameter, which was one of the preprogrammed patterns for ion beam exposure in the FIB machine. For the data analysis, the Ga ion fluence was calculated using the values of ion beam current actually measured. To perform this calculation, the actual current was multiplied by the ion beam exposure time to yield the total number of ions, and this number was divided by the area of the 1- μm circle that, as previously mentioned, was our selected ion beam exposure pattern. We monitored the shape and the lateral size growth of the Pt ball that formed at the free end of the MWNT tip *in situ* using the SEM. The ion beam conditions used are summarized in Table 1. The Pt deposition process and a SEM image of a fabricated Pt ball tip are shown in Fig. 1.

After a Pt ball tip was produced, we transferred the tip onto a sample holder that was specifically prepared to hold an AFM tip for transmission electron microscope (TEM) (300 kV, Tecnai F20S-Twin, FEI Co.) imaging. We performed TEM analysis on the tips thus secured. The composition of the Pt deposits on the Pt ball tips was also analyzed using an energy dispersive spectrometer (EDS) in the TEM.

Table 1
Ion beam conditions used for Pt deposition.

Acceleration voltage (kV)	Nominal current (pA)	Actual current (pA)	Actual Ga ion fluence per 10 nm target thickness (ion/nm^2)
10	3.0	3.8	180
20	23	25.0	160
30	10	7.8	99

3. Results and discussion

Fig. 2 shows SEM pictures of Pt ball growth under a 30 kV 7.8 pA Ga^+ ion beam. We observed that a Pt ball grew at the free end of an MWNT tip as the Pt deposition progressed. When the ball size was small, the ball shape was a spheroid (Fig. 2(b) and (c)), and, with further deposition, the ball shape gradually transformed into an oblate spheroid (Fig. 2(d) and (e)). Finally, when the ball size became too big, the ball developed an irregular shape, and this irregular shape persisted (Fig. 2(f)–(i)). The specifics of the irregular shape development at the final stage of the ball-growing process seemed to be dependent on the growth rate of the Pt ball.¹ The tube diameter also grew slowly at the initial stage of the deposition process (Fig. 2(b)–(g)). However, this growth became faster when the equatorial diameter of the Pt ball exceeded ~ 350 nm (Fig. 2(h) and (i)).

We monitored the growth of the Pt ball and the MWNT tube by their diameters. The equatorial diameter (ball diameter) for the Pt ball and the lateral diameter for the tube (tube diameter) were measured based on SEM images taken after each stage of Pt deposition (Fig. 3). We also calculated the ratio of the ball diameter to the tube diameter. This ratio represents the relative protrusion of the Pt ball out from the MWNT, and the overhang of the CD-AFM tips can be calculated from this ratio and the absolute tube diameter. The overhang controls the maximum reentrance of the sidewall of a line feature that can be measured with such a probe mounted on an AFM. We raised the cumulative total target thickness of Pt deposition up to 1700 nm (with such target thickness, the total ion fluence is approximately $\sim 17,000$ ion/nm^2) in this set of experiments, and the Pt ball diameter grew up to 561 nm.² The rate of increase of the ball/tube diameter ratio significantly decreased when the target thickness reached 900 nm (8900 ion/nm^2). This indicates that the MWNT diameter growth rate increased relative to that of the Pt ball. This may be attributed to additional Pt deposition by a Pt cascade from the ball above to the MWNT as the size of Pt ball reached a threshold. Suppression of Pt deposition on the tube is not easily achievable. However, this effect does not lessen the applicability of Pt ball tips for AFM imaging because such acceleration of tube diameter growth happens when the ball diameter is larger than ~ 300 nm, and the most useful ball diameters for the Pt ball tips are less than 100 nm diameter when the ball maintains a spheroid shape (see Fig. 2).

¹ The irregular shape of the Pt ball developed only when the ball diameter became larger than 100 nm. We believe that the most useful diameter for the Pt ball is less than 100 nm, therefore such irregular shape development should not be a handicap for the usefulness of Pt ball tips. We report the shape change of the Pt ball in the large size limit simply for a complete description of the deposition process.

² If the Pt ball size became much bigger, then the Pt ball collapsed. Often, the factor limiting the maximum Pt ball size was growth of the Pt deposit beneath the Pt ball on the mother AFM tip. Such growth, when grown too large, eventually bridged to the Pt ball above.

We obtained TEM images of six different Pt ball tips, produced with different target thicknesses between 10 and 60 nm, in 10 nm intervals, using a 30 kV 7.8 pA ion beam. We observed that Pt balls formed at the ends of the MWNT tips and that the Pt layer coated the sidewalls of the MWNT below. At both locations (in the ball and on the tube surface), Pt nano-particle aggregates were embedded in an amorphous carbon medium, and formation of a continuous Pt metal layer was not observed. This feature of Pt deposit was also observed in Ref. [20]. On the MWNT, the average Pt particle size was 3–4 nm. We measured the Pt ball and the tube diameter from the TEM images, and plotted them in Fig. 3(a) alongside data obtained from the SEM images of the above-

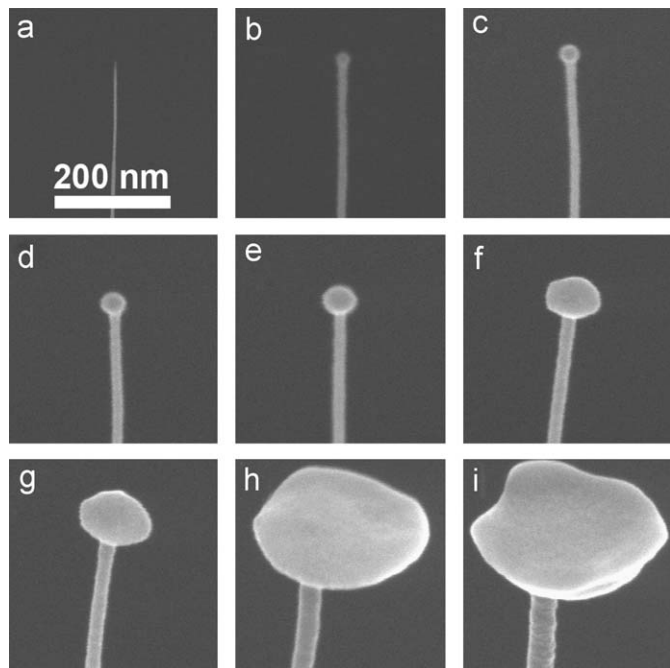


Fig. 2. SEM images of Pt ball growth at the free end of a MWNT tip. After the MWNT was aligned by ion beam (a), Pt was deposited in steps with cumulative target thicknesses of: (b) 20 nm, (c) 40 nm, (d) 60 nm, (e) 100 nm, (f) 200 nm, (g) 300 nm, (h) 800 nm, and (i) 1100 nm. The scale bar is the same for all figures.

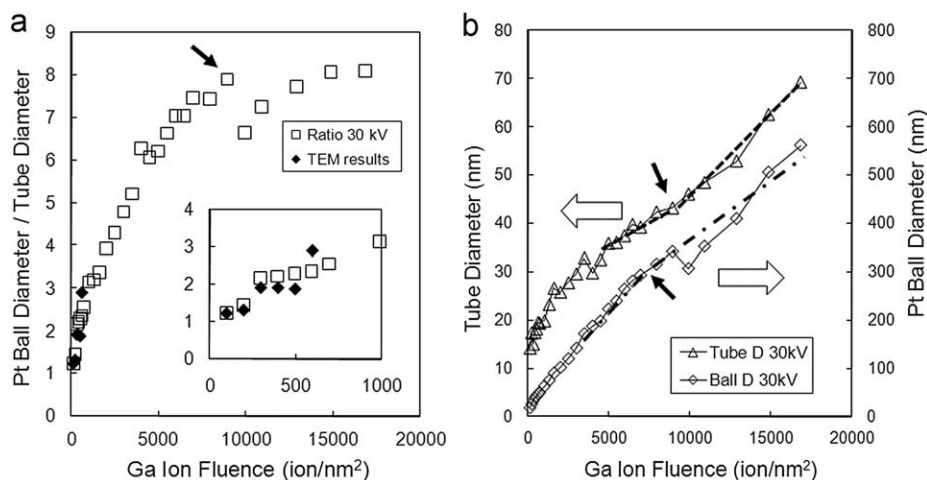


Fig. 3. Size analysis of Pt ball growth under a 30 kV, 7.8 pA Ga ion beam. The ball/tube diameter ratio increased rapidly up to a target thickness of 900 nm (8900 ion/nm², arrow marked) and then the increase slowed (a). The diameter ratios of six different Pt ball tips produced for TEM analysis are also plotted in (a). Their ratio followed the general trend ((a) inset). (b) Ball diameter and tube diameter increases vs. Ga ion fluence; both ball and tube diameters kept increasing until deposition stopped. The tube diameter growth rate increased above the 8900 ion/nm² fluence point (arrow marked), which was the reason why the rate of diameter ratio growth decreased at that point in (a). Dotted lines and dashed-dotted lines are to guide the eye.

mentioned Pt ball growth. The ball/tube diameter ratio from the TEM measurements of six Pt ball tips agreed with the ratios from the SEM measurements of the accumulative growth of one Pt ball tip. This indicates that the Pt ball growth follows a consistent pattern when the ion beam conditions do not change. TEM images of tips that were grown with target thicknesses of 10 and 30 nm are shown in Fig. 4. TEM images of other tips were similar.

EDS analysis was also done during TEM analysis. The results are shown in Fig. 5. The composition of the Pt ball was: 85 atm% C, 10 atm% Pt, 3 atm% Si, and 2 atm% Ga, ignoring the presence of a Cu signal, which originated from the sample holder. Since the percentage of C in EDS is very uncertain, we interpret the percentages as an indication that Pt and C are the dominant constituents of the Pt ball. Pt and C from the precursor gas were deposited together during the Pt deposition, alongside Ga source ions. Si seemed to originate from the sputtered Si of the mother AFM tip. T. Tao et al. [21] deposited Pt on a flat SiO₂ substrate with a 32 kV, 18 pA Ga ion beam and reported similar constituents as ours.

Next, we discuss the reason why the Pt ball is formed at the free top end of the MWNT tip. We start by discussing the mechanism of IBID. For an older and similar deposition technique, EBID, the source that breaks down precursor gas is based on secondary electrons (with a few eV energy), driven from the target material by primary electrons (with a few keV energy) [22]. For IBID, there are two proposed mechanisms. The first possibility is that cascading of the substrate atoms due to the ion source induces the deposition [23,24]. The second possibility is that secondary electrons produced by the ion source induces the deposition [25,26]. Between these two mechanisms, the latter is considered more plausible. Monte-Carlo simulation of the ion trajectory indicated that secondary electrons were more effective in inducing deposition [25], and the material deposition efficiency of the secondary electrons from the ion beam source and from the e-beam source were found to be similar [26]. Therefore, we assume that the source of IBID is secondary electrons.

We also discuss the reason why a bulging Pt ball was formed. We speculate that a combination of the initial round shape of the MWNT tip end, and the incident-angle-dependent generation of the secondary electrons is responsible. When an MWNT is attached to the mother AFM tip by hydrocarbon deposition, the surface of the MWNT is coated with a thin layer of amorphous

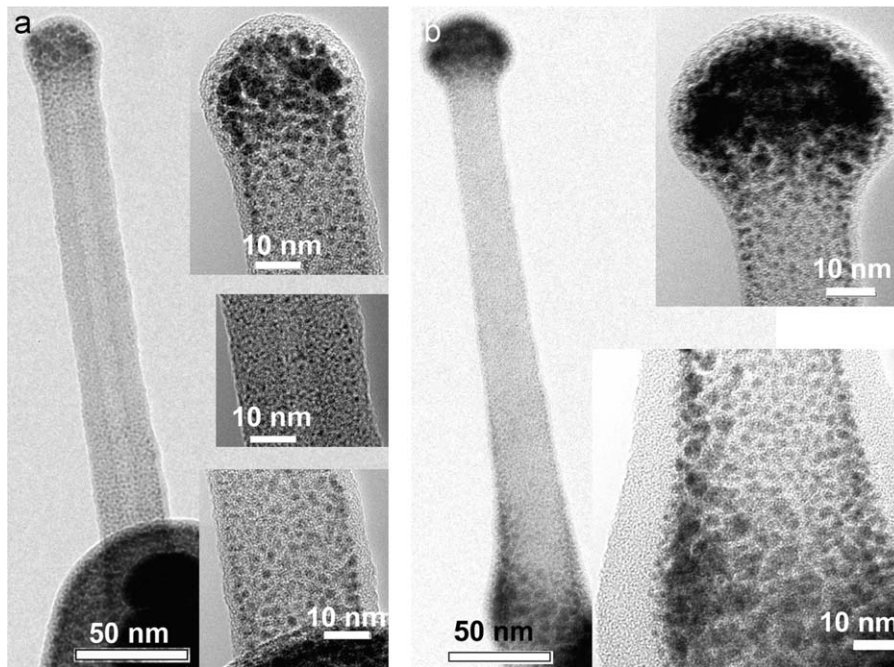


Fig. 4. TEM images of Pt ball tips. Pt deposition target thicknesses were: (a) 10 nm and (b) 30 nm. Pt balls at the free ends of MWNT tips are shown as well as the Pt layer on the MWNT. Insets show high-resolution TEM images. Pt aggregates (dark spots) existed in the ball as well as on the MWNT. They were buried in carbonaceous medium (the grey area surrounding the Pt aggregates).

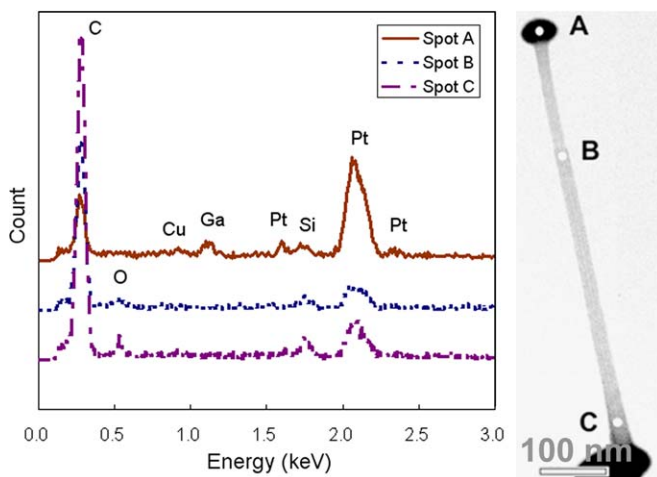


Fig. 5. EDS results at various spots on a Pt ball tip. Spot locations are identified on the right panel. All peaks are identified. Pt was observed at all three spots. The Cu signal was from the sample holder.

carbon, which surrounds the free end of the MWNT [27]. Therefore, the end of the MWNT is closed with amorphous carbon, which usually forms a round shape. It is known that when secondary electrons are generated by an electron beam, the generation yield depends on the angle of incidence (θ) as $1/\cos \theta$. In other words, a tilted surface generates more secondary electrons than does a flat surface [22]. We surmise that a similar angle dependence of the secondary electron yield would happen in the ion beam setup. In fact, we confirmed that such a statement is qualitatively true, as shown in Fig. 6(a)–(c): E-beam-induced secondary electrons were produced more on the angled edge, thus the edge of the ball appeared brighter in the SEM image. A similar effect was observed with ion-beam-induced secondary electrons. Therefore, we confirmed that the generation of secondary electrons by ion beam is more vigorous at the edge of the Pt

ball. Using our assumption that the secondary electrons are the main cause of Pt precursor breakdown during IBID, we deduce that the Pt deposition is more active at the edge. This effect would produce lateral growth of the Pt deposit, forming a spherical ball shape first and then an oblate spheroid ball shape later as the Pt deposition progresses.

Nevertheless, it is also known that the sputtering effect of the Ga ion is more vigorous as the angle of incidence increases [28]. We observed this effect qualitatively as shown in Figs. 6(d) and (e). Because the sputtering is more active at the edge of the Pt ball, the oblate shape became spherical after sputtering.

The net deposition of Pt is a result of competition between these two effects, as expressed below:

$$Y_{\text{net}} = Y_{\text{D}} - S \quad (1)$$

where Y_{net} is the net deposition rate, Y_{D} is the decomposition rate, and S is the sputtering rate [29]. Since we observed that a bulging Pt ball formed and grew, shadowing the MWNT below from the ion beam, we conclude that the net deposition at the edge is more active than on the top of Pt ball. Fig. 6(f) illustrates our proposed mechanism of the Pt ball formation.

Since AFM metrology is the most likely potential application of the Pt ball tips, it is important to know whether a Pt ball tip is strong enough to withstand the stress of AFM imaging. We did an imaging test with one Pt ball tip. Both a Pt-coated conventional Si tip and a Pt ball tip were used to compare images scanned on a patterned Si wafer. The image quality obtained with the Pt ball tip (Fig. 7(a)) was similar to that obtained with a commercial Pt-coated silicon tip (Fig. 7(b)). SEM images of the Pt ball tip before (Fig. 7(c)) and after (Fig. 7(d)) the AFM scan indicated that the Pt ball was strong enough for the use of AFM imaging. Furthermore, comparison of TEM images shown in Fig. 7(e) and (f) to TEM images of other Pt ball tips shown in Fig. 4³ indicate that the Pt

³ Because TEM imaging usually contaminated the Pt ball tips by hydrocarbon deposition during imaging, TEM images of the Pt ball tips were not obtained before the AFM scanning to prevent destruction of the Pt ball tips.

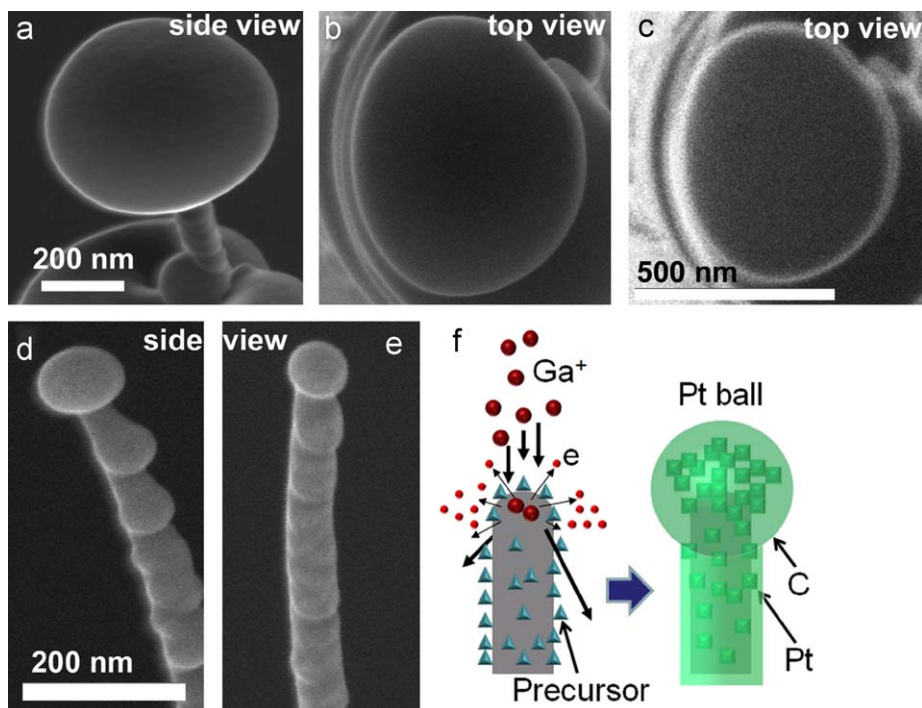


Fig. 6. SEM studies of the mechanism of Pt ball formation. The secondary electron images from a primary e-beam (a) and (b) as well as from an ion beam (c) are shown. For (a) and (b), a 10 kV 130 pA e-beam and for (c), a 30 kV 7.8 pA Ga ion beam were used, respectively. The edges of the Pt ball appear brighter than the rest due to the enhanced production of secondary electrons by the e-beam at the edges in (a) and (b). (a) and (b) have the same scale. A similar image in (c) indicates that the yield of the secondary electrons by ion beam is also higher at the edge. The effectiveness of sputtering increases with the angle of incidence as demonstrated in (d) and (e). The oblate spheroid in (d) became spheroid-shaped in (e) after 40 s sputtering (at 30 kV 33 pA) because the sputtering rate is higher at the edge. (d) and (e) have the same scale. (f) An illustration of the proposed mechanism of the Pt ball formation. As Ga ions collide with the MWNT, secondary electrons are produced more at the edge than on the top. Therefore, the Pt deposits more quickly laterally than vertically, yielding a bulging Pt ball that shadows the MWNT below.

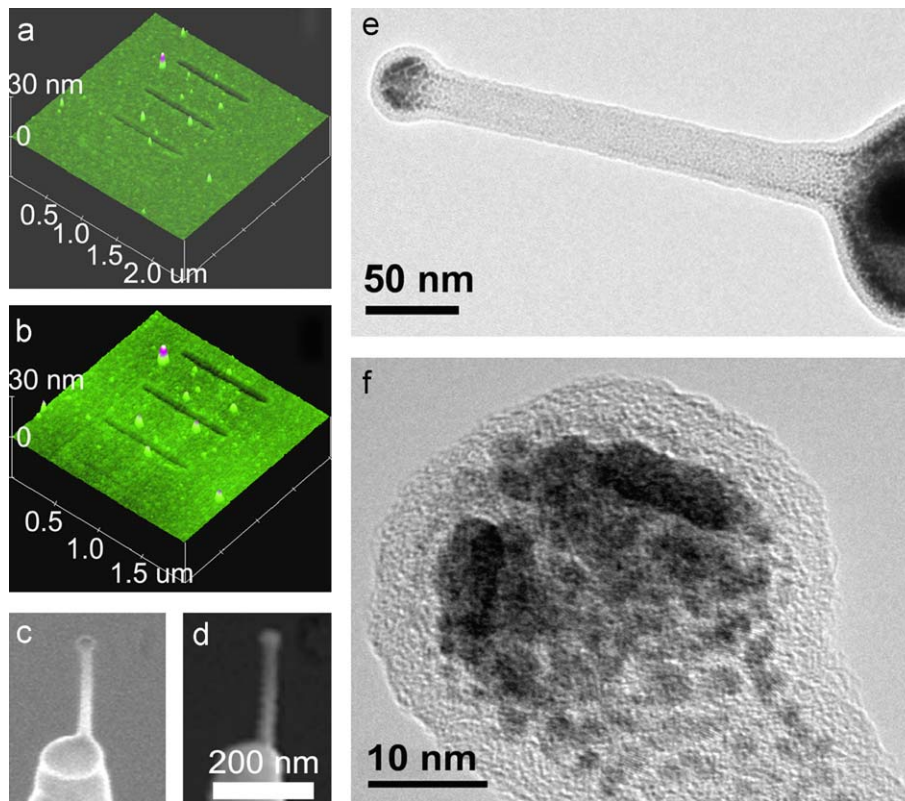


Fig. 7. Results of AFM imaging tests. AFM images of a patterned silicon wafer were obtained by (a) a Pt ball tip and compared with those of (b) a Pt-coated Si tip. With the Pt ball tip, a $2.4 \times 2.4 \mu\text{m}$ area was scanned twice. In each scan, 256×256 pixel data were obtained at a 1 Hz rate. The scan parameters used for the Si tip scan were the same. SEM images obtained before (c) and after (d) the AFM scan, and also TEM images (e, f) of a Pt ball tip after the AFM imaging tests, showed that the Pt ball was intact after AFM imaging. (c) and (d) have the same scale bar. The Pt ball tip was prepared using a 30 kV 7.8 pA ion beam.

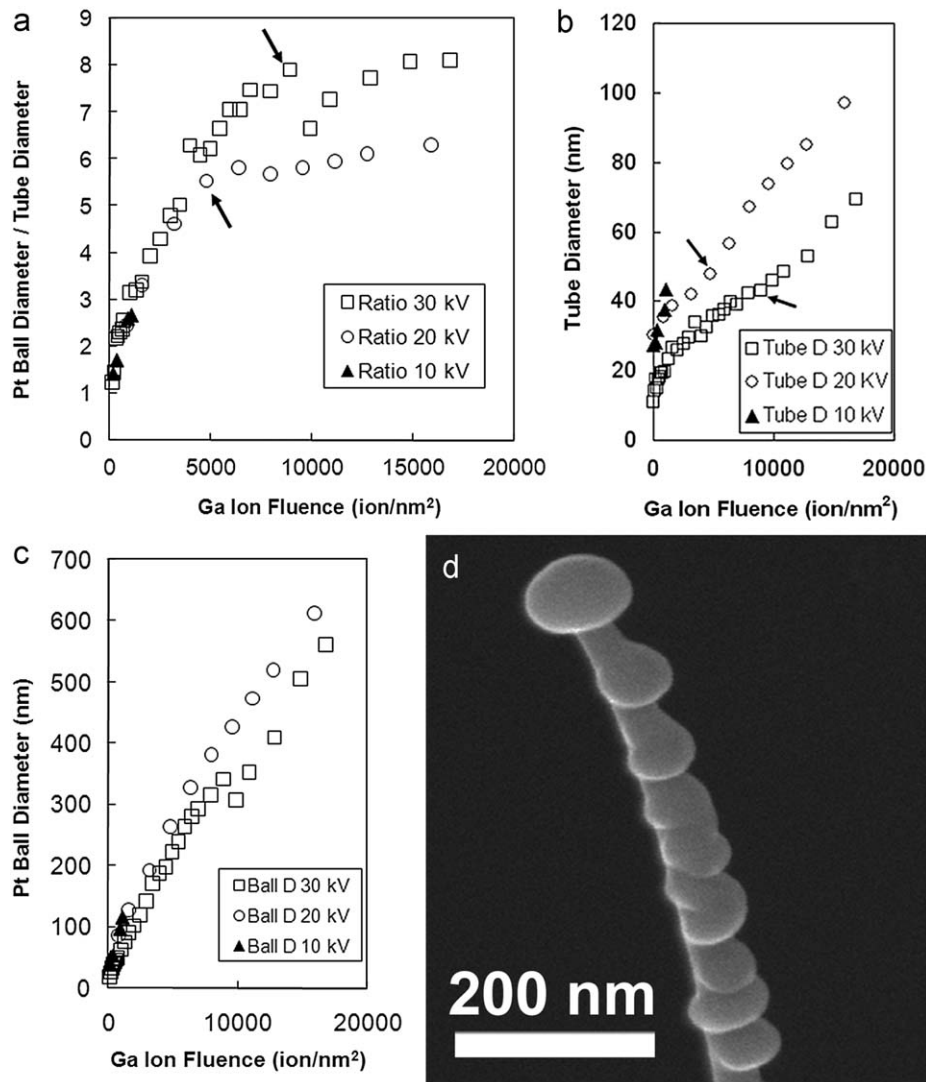


Fig. 8. Comparison of Pt ball growths with 10 kV 3.8 pA, 20 kV 25 pA and 30 kV 7.8 pA ion beams. (a) Growth of the ball/tube diameter ratio. The ratio of this growth under a 20 kV ion beam slowed down around 4800 ion/nm². This slowing happened earlier than it did under the 30 kV ion beam (arrows mark these points). (b) Tube diameter growth under 10, 20 and 30 kV ion beams. Under a 20 kV beam, the tube growth changed slope around 4800 ion/nm² (left arrow) while under a 30 kV beam the change occurred at 8900 ion/nm² (right arrow). (c) Ball diameter growth comparison. The ball growth was similar under the 20 kV and the 30 kV beams. The growth under the 10 kV beam was similar up to the maximum ball size. (d) Pt ball after a 60 nm Pt target thickness was deposited with the 10 kV ion beam. With the 10 kV beam, MWNT alignment was difficult to maintain during deposition, as the MWNT continued to bend towards the left, and therefore the Pt ball could be grown only up to ~116 nm size.

ball tip did not undergo any significant deformation during the imaging. Thus, the Pt ball tip was able to withstand the AFM imaging stress.

Lastly, we report Pt ball growth under different ion beam conditions. As mentioned in Section 2, we used 10 kV, 3.8 pA and 20 kV, 25 pA Ga ion beams, as well as a 30 kV, 7.8 pA ion beam, and observed the Pt ball growth. Results are shown in Fig. 8. The Pt ball grew up to 613 nm under a 20 kV beam, and up to 116 nm under a 10 kV beam. We observed that Pt ball growth under the 30 kV ion beam initially progressed similarly, in terms of the ball/tube diameter ratio, to growth under 10 and 20 kV ion beams. With a 20 kV beam, the largest ratio observed was 6.3. Growth of this ratio changed its slope similarly to the growth with 30 kV ion beam (Fig. 8(a)). This slope change also happened because the growth rate of the tube diameter with the 20 kV ion beam increased at a particular point (Fig. 8(b)). The diameter ratio changed its slope at an earlier point with the 20 kV beam than with the 30 kV beam. This may mean that the 30 kV beam is more suitable for producing more highly protruding Pt ball tips. Ball diameter growth was similar in every case except the one with

10 kV ion beam (Fig. 8(c)). With the 10 kV ion beam, MWNT alignment was difficult to maintain during the Pt ball growth. Although at the beginning the MWNT was aligned toward the ion beam, it kept pointing downward while the Pt was depositing (Fig. 8(d)). Therefore, with the 10 kV ion beam, the Pt ball reached a maximum equatorial diameter of only 116 nm. The mechanism behind this downward tube bending under a 10 kV ion beam is not yet clearly understood. Investigation of the mechanism is an interesting subject inviting further serious research efforts and is beyond the scope of this paper.

4. Conclusion

We report a novel fabrication method to produce nano-balls attached AFM tips using IBID of Pt. The diameter of the balls could be finely controlled up to ~600 nm and the ball/tube diameter ratio could be adjusted up to 8. Using TEM and EDS analyses, we showed that the attached Pt balls are aggregated Pt nanoparticles. We also tested a Pt ball tip for AFM imaging and found

that the Pt ball was strong enough for this application. Our production method for nano-scale Pt ball tips may increase the application range of AFM metrology.

Acknowledgments

The authors thank Ms. Kyung Jin Park and Mr. Yun Chang Park at the National Nanofab Center for their assistance in operating the FIB and the TEM. This work was financially supported in part by the Korean National Program for Tera-level Nanodevices and in part by Seoul Research & Business Development Program (WR090671).

References

- [1] H. Dai, J.H. Hafner, A.G. Rinzier, D.T. Colbert, R.E. Smalley, *Nature* 384 (1996) 147–150.
- [2] H. Nishijima, S. Kamo, S. Akita, Y. Nakayama, K.I. Hohmura, S.H. Yoshimura, K. Takeyasu, *Appl. Phys. Lett.* 74 (1999) 4061–4063.
- [3] J. Martinez, T.D. Yuzvinsky, A.M. Fennimore, A. Zettl, R. Garcia, C. Bustamante, *Nanotechnology* 16 (2005) 2493–2496.
- [4] H.-C. Liu, D. Fong, G.A. Dahlen, M. Osborn, S. Hand, J.R. Osborne, *Proc. SPIE* 6152 (2006) 61522Y.
- [5] Y. Martin, H.K. Wickramasinghe, *Appl. Phys. Lett.* 64 (1994) 2498–2500.
- [6] B.C. Park, K.Y. Jung, W.Y. Song, B.-H. O, S.J. Ahn, *Adv. Mater.* 18 (2006) 95–98.
- [7] D.-H. Kim, J. Choi, Y.H. Kahng, S.J. Ahn, B.C. Park, *J. Appl. Phys.* 101 (2007) 064317-1–064317-8.
- [8] B.C. Park, J.H. Choi, S.J. Ahn, D.-H. Kim, L. Joon, R. Dixon, G. Orji, J. Fu, T. Vorbürger, *Proc. SPIE* 6518 (2007) 651819-1–651819-14.
- [9] E.-S. Yoon, R.A. Singh, H.-J. Oh, H. Kong, *Wear* 259 (2005) 1424–1431.
- [10] C. LaTorre, B. Bhushan, *Ultramicroscopy* 106 (2006) 720–734.
- [11] B. Bhushan, *Wear* 251 (2001) 1105–1123.
- [12] I.-H. Sung, H.-S. Lee, D.-E. Kim, *Wear* 254 (2003) 1019–1031.
- [13] M. Nosonovsky, B. Bhushan, *Mater. Sci. Eng. R Rep.* 58 (2007) 162–193.
- [14] S.E. Cross, Y.-S. Jin, J. Rao, J.K. Gimzewski, *Nat. Nanotech.* 2 (2007) 780–783.
- [15] K. Gamo, N. Takakura, N. Samoto, R. Shimizu, S. Namba, *Jpn. J. Appl. Phys.* 23 (1984) L293–L295.
- [16] J.-Y. Igaki, K. Kanda, Y. Haruyama, M. Ishida, Y. Ochiai, J.-I. Fujita, T. Kaito, S. Matsui, *Microelectron. Eng.* 83 (2006) 1225–1228.
- [17] S. Matsui, T. Kaito, J.-I. Fujita, M. Komuro, K. Kanda, Y. Haruyama, *J. Vac. Sci. Technol. B* 18 (2000) 3181–3184.
- [18] T. Hoshino, K. Watanabe, R. Kometani, T. Morita, K. Kanda, Y. Haruyama, T. Kaito, J. Fujita, M. Ishida, Y. Ochiai, S. Matsui, *J. Vac. Sci. Technol. B* 21 (2003) 2732–2736.
- [19] W.Y. Song, K.Y. Jung, B.-H. O, B.C. Park, *Rev. Sci. Instrum.* 76 (2005) 025107-1–025107-4.
- [20] R.M. Langford, T.-X. Wang, D. Ozkaya, *Microelectron. Eng.* 84 (2007) 784–788.
- [21] T. Tao, J.S. Ro, J. Melngailis, *J. Vac. Sci. Technol. B* 8 (1990) 1826–1829.
- [22] K.T. Kohlmann-von Platen, J. Chiebek, M. Weiss, K. Reimer, H. Oertel, W.H. Brüngrer, *J. Vac. Sci. Technol. B* 11 (1993) 2219–2223.
- [23] A.D. Dubner, A. Wagner, J. Melngailis, C.V. Thompson, *J. Appl. Phys.* 70 (1991) 665–673.
- [24] J.S. Ro, C.V. Thompson, J. Melngailis, *J. Vac. Sci. Technol. B* 12 (1994) 73–77.
- [25] P.W.H. de Jager, C.W. Hagen, P. Kruit, *Microelectron. Eng.* 30 (1996) 353–356.
- [26] S. Lipp, L. Frey, C. Lehrer, E. Demm, S. Pauthner, H. Ryssel, *Microelectron. Reliab.* 36 (1996) 1779–1782.
- [27] Y.H. Kahng, J. Choi, B.C. Park, D.-H. Kim, J.H. Choi, J. Lyou, S.J. Ahn, *Nanotechnology* 19 (2008) 195705-1–195705-7.
- [28] L. Frey, C. Lehrer, H. Ryssel, *Appl. Phys. A* 76 (2003) 1017–1023.
- [29] A.D. Dubner, A. Wagner, *J. Appl. Phys.* 66 (1989) 870–874.